Neutron transition densities for low lying states in ^{58}Ni obtained by using 200 MeV inelastic proton scattering

J. Lisantti
Centenary College of Louisiana, Shreveport, Louisiana 71134

A. D. Bacher, G. P. A. Berg, S. M. Bowyer,* S. Chang,† J. Liu,‡ C. Olmer, E. J. Stephenson, S. P. Wells,§ and S. W. Wissink
Indiana University Cyclotron Facility, Bloomington, Indiana 47408

K. H. Hicks
Ohio University, Athens, Ohio 45701
(Received 28 May 1998)

Differential cross section and analyzing power measurements have been made for 200 MeV inelastic proton scattering from ^{58}Ni. Using the code LEA, neutron transition densities have been obtained for four 2^+, one 3^-, and five 4^+ low lying states. Charge transition densities obtained from electron scattering were used in order to minimize the nuclear structure uncertainty, along with a recent 200 MeV empirical effective interaction. Two types of calculations have been used in comparison to the data, one in which the neutron transition densities are obtained by scaling the charge transition densities by N/Z, the other in which the neutron transition densities are allowed to vary to obtain a best fit to the data. Multipole matrix elements are obtained and compared to collective model analyses using both intermediate energy protons and pion scattering results. The radial shapes of the neutron transition densities for the lowest lying 2^+ and 3^- states are compared to those calculated using the energy density method. [S0556-2813(98)06810-1]

PACS number(s): 25.40.Ep, 27.40.+z

I. INTRODUCTION

The radial shape and overall strength of both neutron and proton transition densities can be used as an important test of various models of the nucleus. Inelastic electron scattering for many years has been used to obtain charge transition densities [1]. Unfortunately, electron scattering cannot be used to obtain neutron transition densities since the electron interacts only very weakly with neutrons in the nucleus. Therefore, hadron scattering must be employed to obtain neutron transition densities. Until recently, the use of hadron scattering to obtain neutron transition densities was plagued by the lack of an adequate hadron-nucleus interaction. Without such an interaction it is not possible to unfold the effect of neutron density from the interaction. Recently, Kelly and co-workers have completed a program aimed at determining empirical effective interactions for intermediate energy proton-nucleus scattering [2–8]. These empirical interactions, which are obtained from examining states in self-conjugate nuclei such as ^{16}O and ^{40}Ca, are then used along with charge transition densities obtained from electron scattering to determine neutron transition densities for a variety of nuclei. Neutron transition densities have already been obtained for low lying natural parity states in ^{18}O [9], ^{30}Si [10], ^{34}S [11], ^{48}Ca [12], and ^{88}Sr [13]. In this paper we report the extraction of neutron transition densities for four 2^+, one 3^-, and five 4^+ states in ^{58}Ni in a manner similar to Refs. [9–13].

In Sec. II we will briefly describe the experimental setup for the inelastic proton scattering measurements. Section III contains a description of the model inputs and fitting procedures. Section IV presents the data and the resulting neutron transition densities. Section V summarizes the results and presents the conclusions.

II. EXPERIMENT

The experiment was carried out at the Indiana University Cyclotron Facility (IUCF) using 199.0 MeV protons polar-

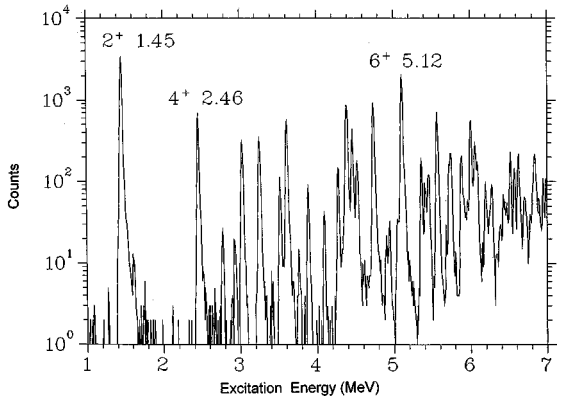

FIG. 1. Excitation energy spectrum for 199.0 MeV spin up protons scattered at 40.0° from ^{58}Ni.

*Present address: Pacific Northwest Laboratories, Batelle Memorial Institute, Richland, WA 99352.

†Present address: IBM Corporation, One IBM Plaza, Chicago, IL 60611.

‡Permanent address: Shell E&P Technology Center, Houston, TX 77025.

§Present address: Louisiana Tech, Dept. of Physics, Ruston, LA 71272.

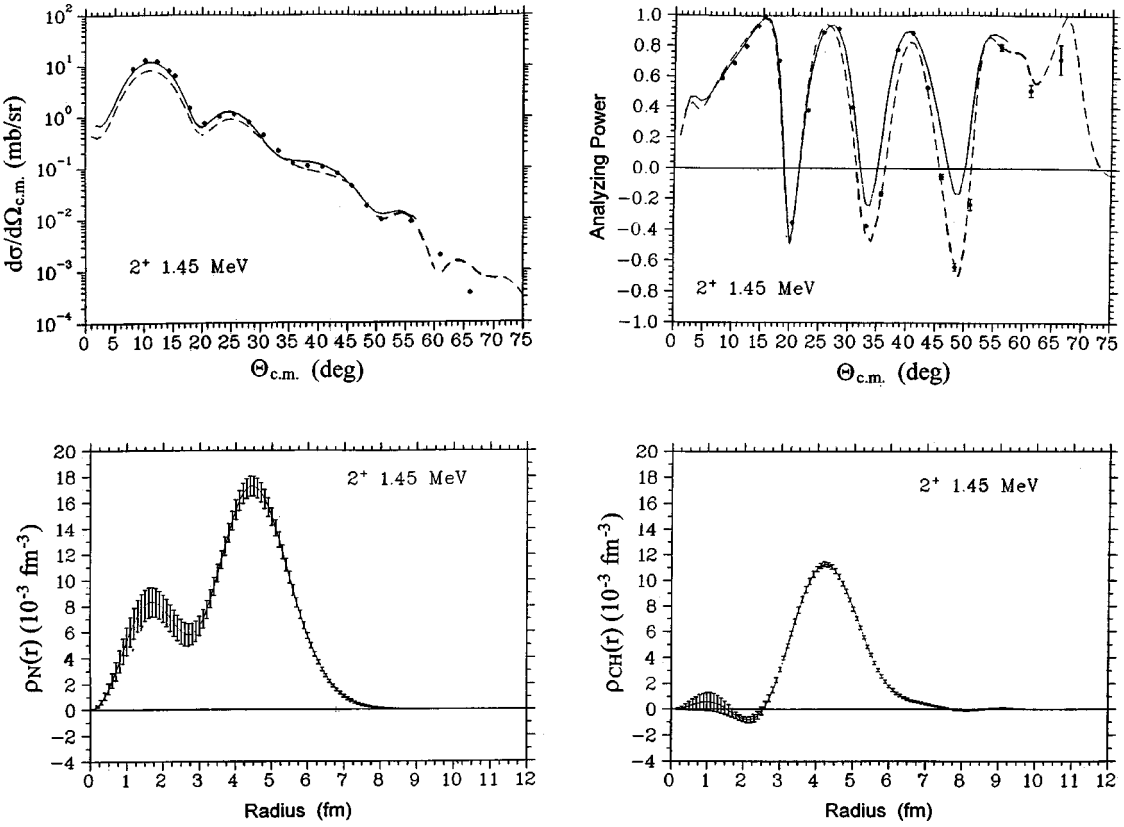

FIG. 2. Cross section and analyzing power data for the 2^+ state at 1.45 MeV, along with the neutron transition density derived in this work, and the charge transition density from inelastic electron scattering from Ref. [16]. The dashed curves are the result of using a neutron transition density that is obtained by scaling the charge transition density by N/Z. The solid curve is the result of allowing the neutron transition density to vary to provide a best fit to the data.

ized in the direction normal to the scattering plane. The scattered protons were detected by the K600 magnetic spectrometer [14,15]. The energy resolution for this experiment was 25–30 keV for most of the data taken. A typical spectrum is shown in Fig. 1. Our measurements extend from the elastic peak up to approximately 15 MeV of excitation energy; however, in this paper we examine states up to an excitation energy of 4.75 MeV, which is the limit of the available electron scattering data on 2^+, 3^-, and 4^+ states [16].

Forward angle measurements were taken at 8°, 10°, 12°, 14°, 15°, and 17.75° using a Faraday cup internal to the spectrometer scattering chamber. Using an external Faraday cup and beam dump, measurements were taken from 15° to 50° in 2.5° steps, and at 55°, 60°, and 65°. The target was a rolled foil of 99.9% ^{58}Ni with a thickness of 3.1 mg/cm^2. The beam current on target varied from 1 to 130 nA depending upon the angle of the spectrometer. The beam current was adjusted so that the live time of the electronics and acquisition computer was always larger than 90%. The angle calibration of the spectrometer was measured by using a composite natural C and ^{58}Ni target and by measuring the kinematic crossover of the elastic peak of ^{12}C with the 1.45 MeV, 2^+ state in ^{58}Ni. Using this method, the uncertainty in our laboratory scattering angle is approximately $\pm 0.1°$. The solid angle of the spectrometer depended on the size of the entrance apertures employed. Two apertures were used, one was a 0.93-cm hole giving a solid angle of 0.145 ± 0.001 msr; the other was a rounded slot 2.54 cm on a side, giving a solid angle of 1.17 ± 0.01 msr. Beam polarization was continuously monitored using p-d in-beam polarimeters [17]. Differences between spin up and down polarization magnitudes were periodically checked by using a p-^{4}He polarimeter which is inserted into the beam line between the injector and main stage cyclotron. The magnitude of the polarization varied from 0.69 to 0.75 throughout the experiment.

The normalizations obtained using the information above were then used to calculate absolute cross sections and analyzing powers. Our normalization procedures were checked by performing an optical model parameter search on the elastic scattering data obtained during the experiment for ^{58}Ni. These parameters were then used in a deformed optical model calculation using ECIS79 to obtain the hadronic deformation length δ_H for the 1.45 MeV, 2^+ state. Previous work on ^{58}Ni has shown that δ_H for this state does not vary with incident proton beam energy (178–1047 MeV) and that $\delta_H = 0.82 \pm 0.04$ [18]. The value for δ_H determined in the present analysis is 0.84, which lends credence to our absolute cross section measurements.

The energy calibration of the focal plane was determined by using well-known states as reference energies and fitting the spectra at each angle up to a quadratic term in momentum. Using this method, the excitation energies are reliable to ± 15 keV up to approximately 10 MeV; for the higher excitation energies, this value is ± 30 keV.

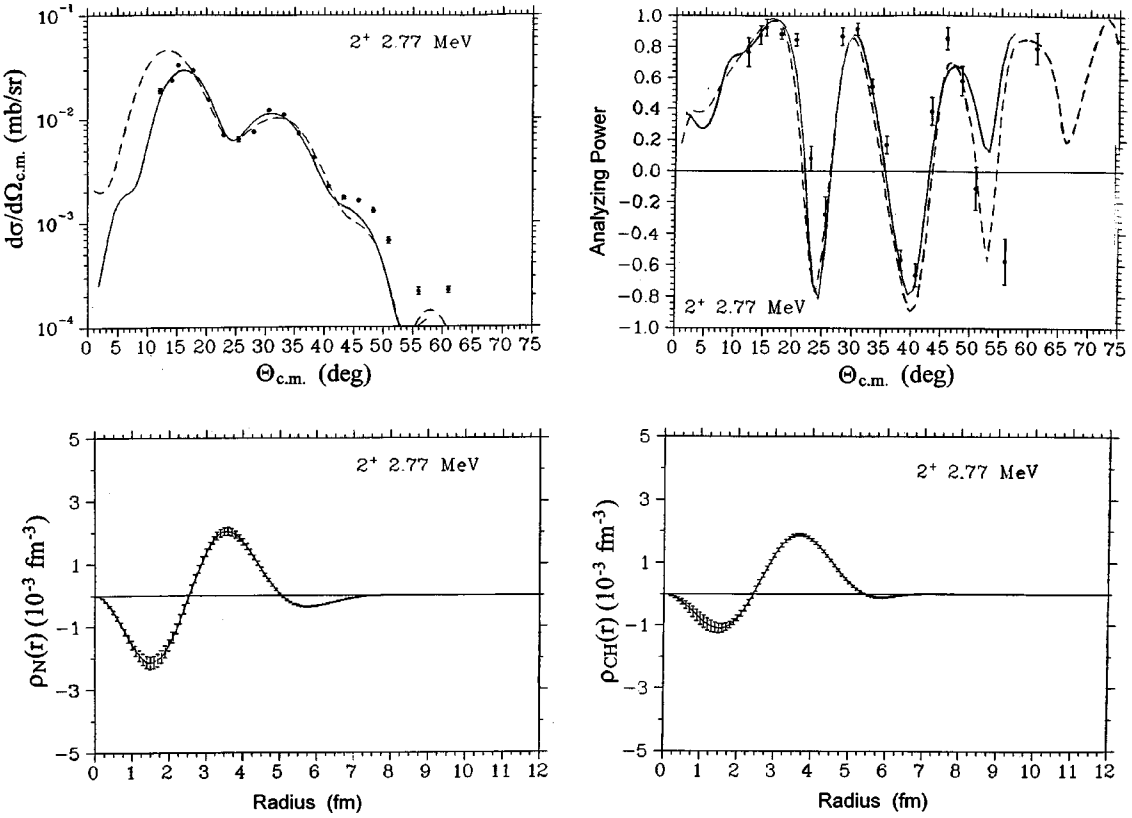

FIG. 3. Cross section and analyzing power data for the 2^+ state at 2.77 MeV, figure description the same as Fig. 2.

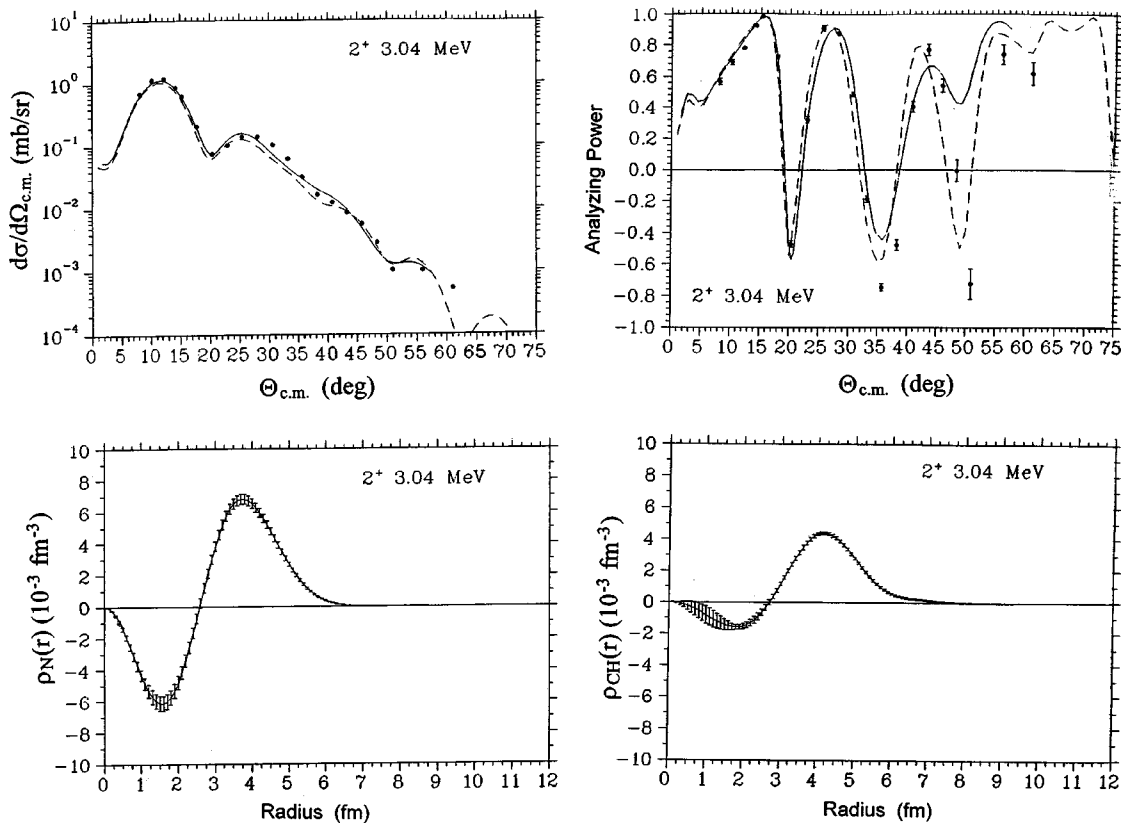

FIG. 4. Cross section and analyzing power data for the 2^+ state at 3.04 MeV, figure description the same as Fig. 2.

TABLE I. Laguerre-Gaussian expansion coefficients for the best-fit neutron transition densities.

a_n	2_1^+, 1.45 MeV	2_2^+, 2.77 MeV	2_3^+, 3.04 MeV
1	$(4.540\pm0.285)\times10^{-2}$	$(2.773\pm0.325)\times10^{-3}$	$(1.086\pm0.086)\times10^{-2}$
2	$(-2.904\pm0.140)\times10^{-2}$	$(-2.887\pm0.187)\times10^{-3}$	$(-1.294\pm0.060)\times10^{-2}$
3	$(1.648\pm0.075)\times10^{-2}$	$(-1.230\pm0.080)\times10^{-3}$	$(-3.596\pm1.520)\times10^{-4}$
4	$(-1.293\pm0.222)\times10^{-3}$	$(4.516\pm0.404)\times10^{-4}$	$(5.225\pm0.701)\times10^{-5}$
5	$(-6.8600\pm2.023)\times10^{-4}$	$(4.029\pm1.834)\times10^{-5}$	$(5.871\pm2.152)\times10^{-5}$
6	$(-1.472\pm1.015)\times10^{-4}$	$(-4.081\pm1.057)\times10^{-5}$	$(-2.449\pm1.118)\times10^{-5}$
	2_4^+, 3.26 MeV	3_1^-, 4.47 MeV	4_1^+, 2.46 MeV
1	$(2.456\pm0.133)\times10^{-2}$	$(2.829\pm0.153)\times10^{-2}$	$(1.066\pm0.046)\times10^{-2}$
2	$(-1.245\pm0.062)\times10^{-2}$	$(-1.233\pm0.062)\times10^{-2}$	$(-3.611\pm0.202)\times10^{-3}$
3	$(-6.185\pm1.664)\times10^{-4}$	$(5.549\pm1.160)\times10^{-4}$	$(-2.737\pm0.413)\times10^{-4}$
4	$(4.096\pm0.906)\times10^{-4}$	$(6.313\pm6.757)\times10^{-5}$	$(5.126\pm2.708)\times10^{-5}$
5	$(6.230\pm2.927)\times10^{-5}$	$(2.060\pm0.297)\times10^{-4}$	$(1.181\pm0.165)\times10^{-4}$
6	$(-1.792\pm1.427)\times10^{-5}$	$(-1.054\pm0.189)\times10^{-4}$	$(6.039\pm8.217)\times10^{-6}$
	4_2^+, 3.62 MeV	4_3^+, 4.29 MeV	4_4^+, 4.40MeV
1	$(7.990\pm0.470)\times10^{-3}$	$(4.410\pm0.240)\times10^{-3}$	$(9.688\pm0.493)\times10^{-3}$
2	$(-1.962\pm0.129)\times10^{-3}$	$(-1.116\pm0.089)\times10^{-3}$	$(-3.098\pm0.159)\times10^{-3}$
3	$(-3.990\pm0.423)\times10^{-3}$	$(-5.407\pm1.445)\times10^{-5}$	$(-8.554\pm0.846)\times10^{-4}$
4	$(-1.223\pm27.41)\times10^{-6}$	$(5.710\pm0.923)\times10^{-5}$	$(-2.227\pm0.674)\times10-4$
5	$(7.451\pm1.790)\times10^{-5}$	$(6.946\pm2.366)\times10^{-6}$	$(-4.015\pm4.214)\times10^{-5}$
6	$(2.115\pm0.765)\times10^{-5}$	$(-7.271\pm1.687)\times10^{-6}$	$(-1.634\pm1.465)\times10^{-5}$
	4_5^+, 4.75 MeV		
1	$(1.354\pm0.079)\times10^{-2}$		
2	$(-3.317\pm0.183)\times10^{-3}$		
3	$(-5.944\pm0.599)\times10^{-4}$		
4	$(-8.252\pm39.67)\times10^{-6}$		
5	$(1.224\pm0.281)\times10^{-4}$		
6	$(3.863\pm1.241)\times10^{-5}$		

III. CALCULATIONS

A. Distorted wave calculations

All of the calculations were performed using the code LEA (linear expansion analysis) [2–13,19]. Details about this code can be located in Refs. [2–13]. We will present only those details of the code that are relevant for our calculations. The ground-state charge density (used to generate optical potentials) was obtained from Ref. [20] using the Fourier-Bessel coefficients presesented in Ref. [21]. The neutron ground-state densities employed are the ground-state charge densities scaled by N/Z. The charge transition densities were obtained from inelastic electron scattering [16,22] and have also been parametrized as Fourier-Bessel coefficients. The proton transition densities were unfolded from the charge transition densities. The knock-on exchange was handled using the zero-range approximation in LEA. The Cheon rearrangement factor [23] was used in all of the inelastic calculations. Coulomb excitation was included in the calculations for all of the excitations. The density dependence was incorporated in all of the calculations using the local density approximation which has been shown to be valid for intermediate energy proton scattering [3,8].

Both the optical and inelastic scattering potentials were obtained by employing the same empirical effective interaction. The interaction used was the PH3 parameter set as listed in Table II of Ref. [8]. This empirical interaction was obtained by simultaneously fitting both ^{16}O and ^{40}Ca 200 MeV data for well-known low lying states and is based on the Paris-Hamburg interaction which has been shown to give a good description of intermediate energy proton scattering from ^{58}Ni [24]. The PH3 parameters are similar to the parameters given in Ref. [25] which also fit ^{16}O and ^{40}Ca data simultaneously at 200 MeV. A recent paper [12] on obtaining neutron transition densities for ^{48}Ca using 200 and 318 MeV polarized protons studied the effect of using different empirical effective interactions in the extraction of neutron transition densities. The differences in the neutron transition densities obtained using the PH3 interaction or the LR3 interaction (Love-Ray, Table II of Ref. [8]) were between 6% and 18% for the peak of the transition densities and between 3% and 11% for the integral moments. Reference [12] con-

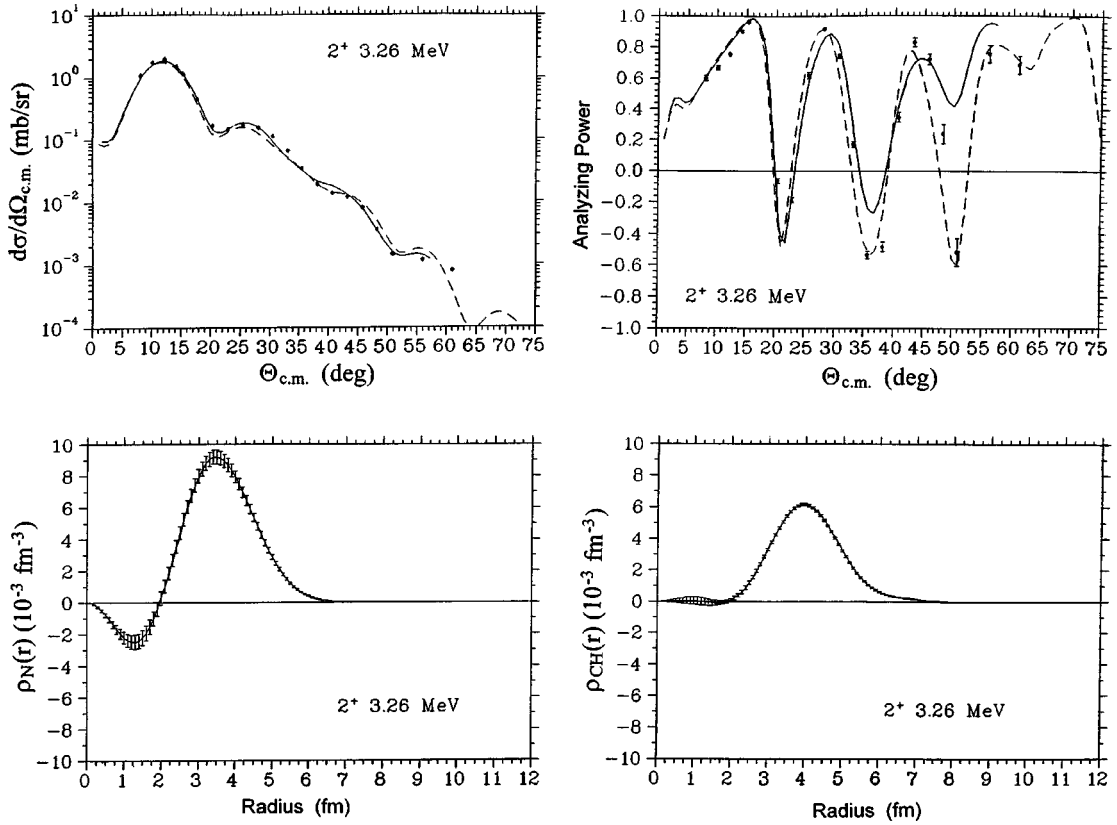

FIG. 5. Cross section and analyzing power data for the 2^+ state at 3.26 MeV, figure description the same as Fig. 2.

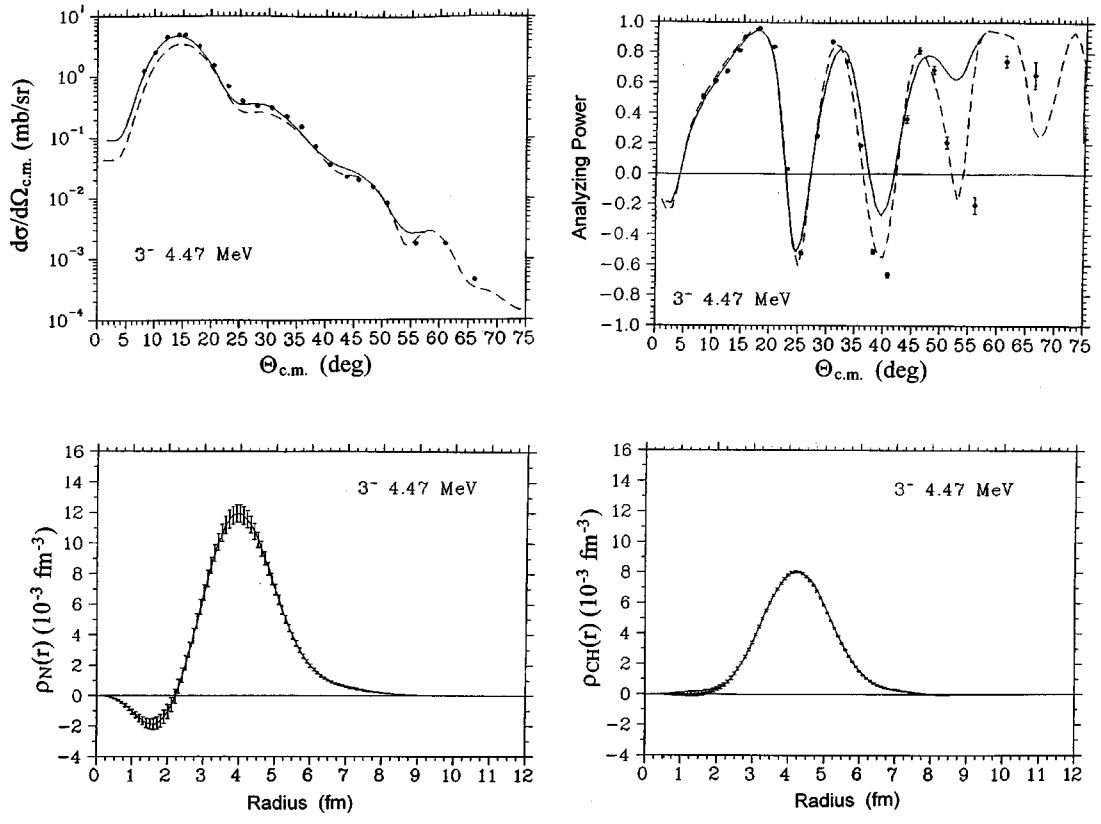

FIG. 6. Cross section and analyzing power data for the 3^- state at 4.47 MeV, figure description the same as Fig. 2.

TABLE II. Neutron and proton multipole matrix elements extracted for states in ^{58}Ni.

State	M_n[a]	M_p[a]	M_n/M_p[a]	M_n/M_p[b]	M_n/M_p[c]	M_n/M_p[d]
2_1^+	24.37±0.83	12.51	1.94±0.07	1.07±0.12	1.29±0.05	1.40
2_2^+	−0.081±0.102	0.706	−0.11±0.16			
2_3^+	4.11±0.19	3.947	1.04±0.05	0.86±0.23	0.95±0.04	
2_4^+	5.09±0.22	5.057	1.01±0.04	0.81±0.19	0.96±0.21	
3_1^-	71.43±2.61	48.74	1.47±0.05	0.70±0.17	0.95±0.12	1.39
4_1^+	232.7±10.2	113.46	2.05±0.09	0.91±0.33	1.15±0.37	
4_2^+	97.69±7.26	125.14	0.78±0.06	0.46±0.19		
4_3^+	58.76±4.09	96.22	0.61±0.04			
4_4^+	134.0±8.57	107.00	1.25±0.08			
4_5^+	170.9±10.8	126.26	1.35±0.09	0.98±0.20		

[a]Present work, calculated using LEA, 5% uncertainty assigned to M_p for the calculation of M_n/M_p.
[b]Reference [18] proton scattering results.
[c]Reference [27] proton scattering results.
[d]Reference [28] pion scattering results.

cludes that the use of these different interactions does not significantly alter the extracted neutron transition densities.

B. Extraction of neutron transition densities

The radial form of the neutron transition densities, $\rho_N(r)$, is represented by the Laguerre-Gaussian expansion (LGE)

$$\rho_N(r) = x^L e^{-x^2} \Sigma a_n L_n^{L+1/2}(2x^2), \qquad (1)$$

where $x = r/b$, with the harmonic oscillator parameter $b = 2.20$ fm for ^{58}Ni; L represents the multipolarity of the excitation from the ground state ($L = 0$). The terms inside the sum are the Laguerre polynomials with expansion coefficients a_n. It is these expansion coefficients that are varied in order to simultaneously fit the cross section and analyzing power data.

Examination of the charge transition densities shows that some of them oscillate at radii far beyond the edge of the

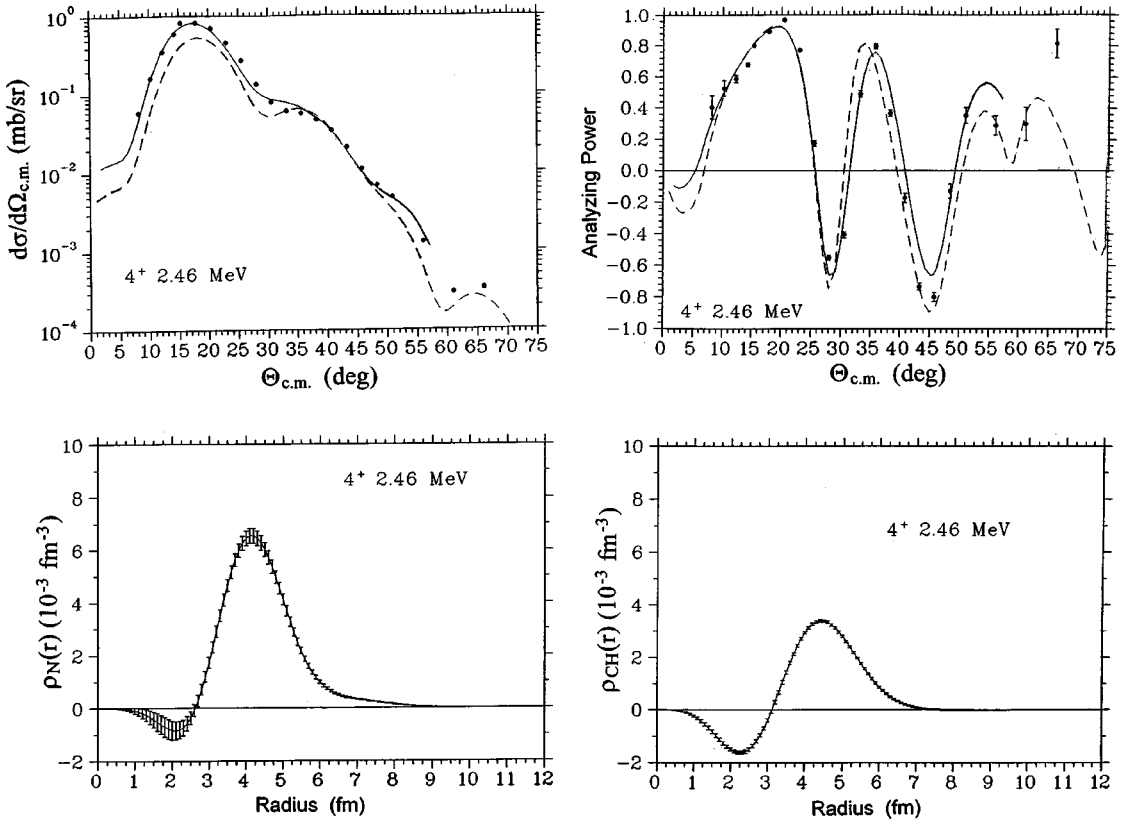

FIG. 7. Cross section and analyzing power data for the 4^+ state at 2.46 MeV, figure description the same as Fig. 2.

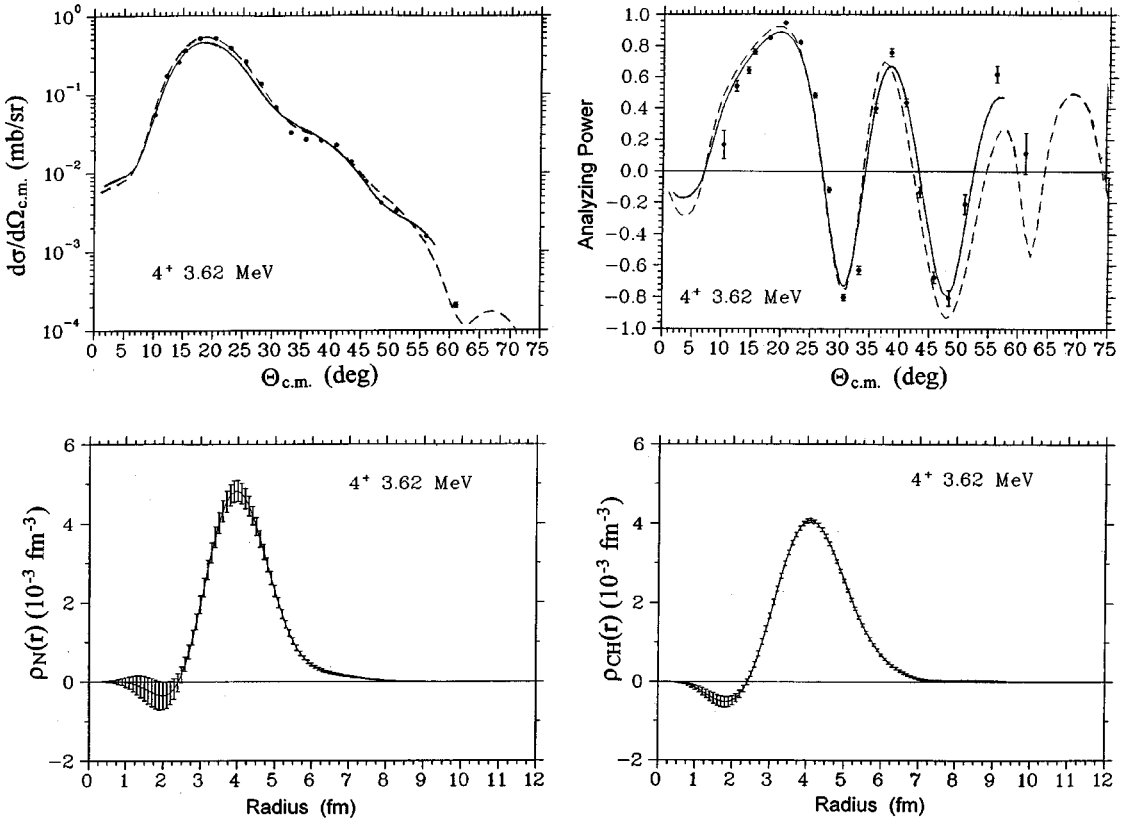

FIG. 8. Cross section and analyzing power data for the 4^+ state at 3.62 MeV, figure description the same as Fig. 2.

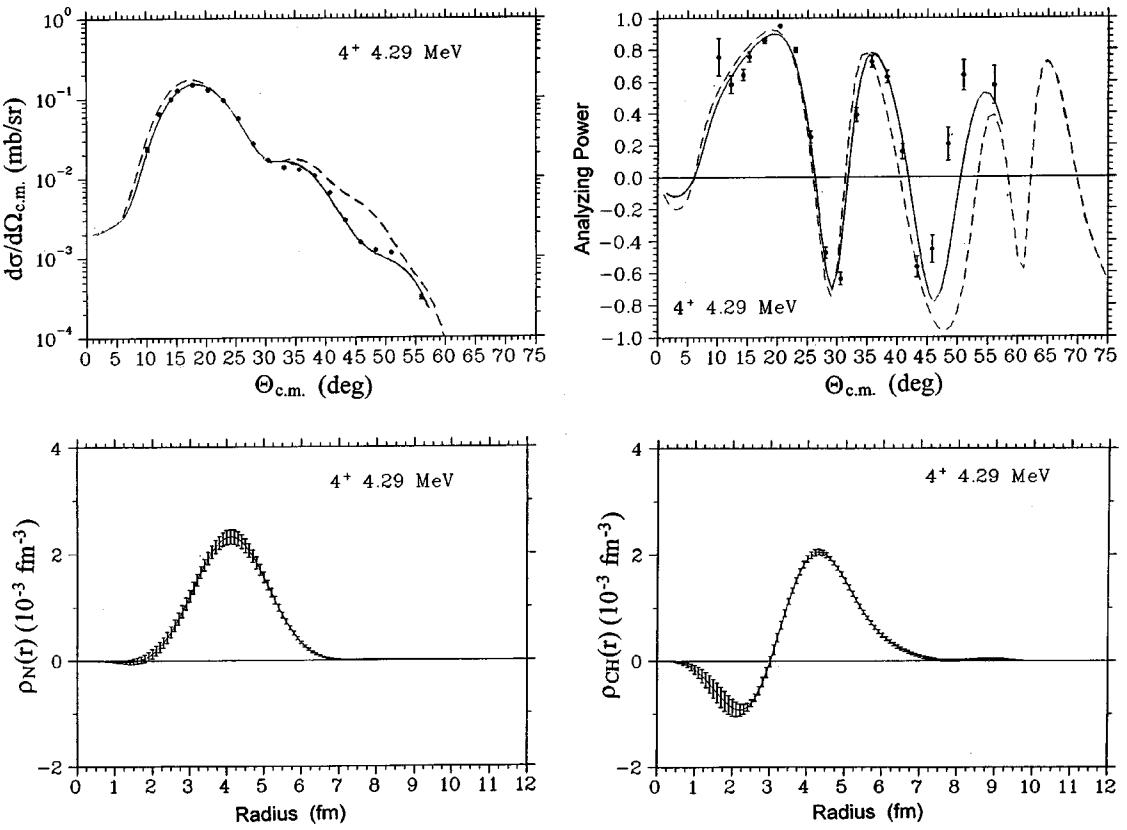

FIG. 9. Cross section and analyzing power data for the 4^+ state at 4.29 MeV, figure description the same as Fig. 2.

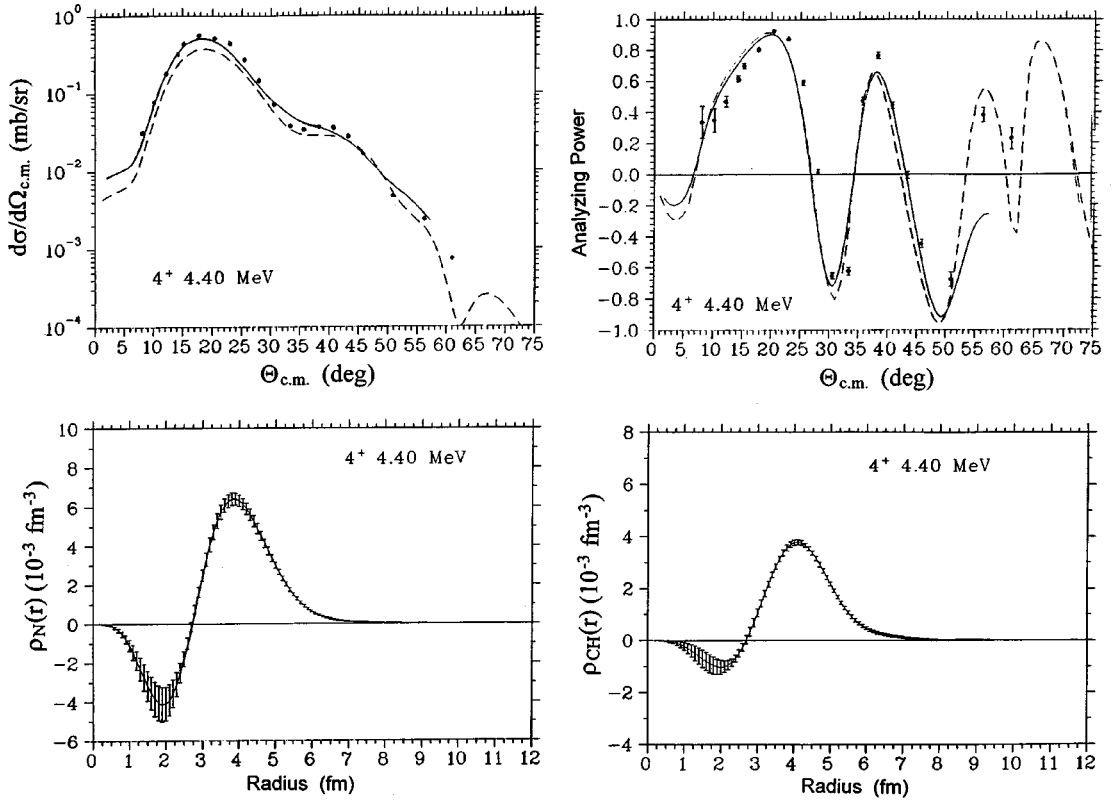

FIG. 10. Cross section and analyzing power data for the 4^+ state at 4.40 MeV, figure description the same as Fig. 2.

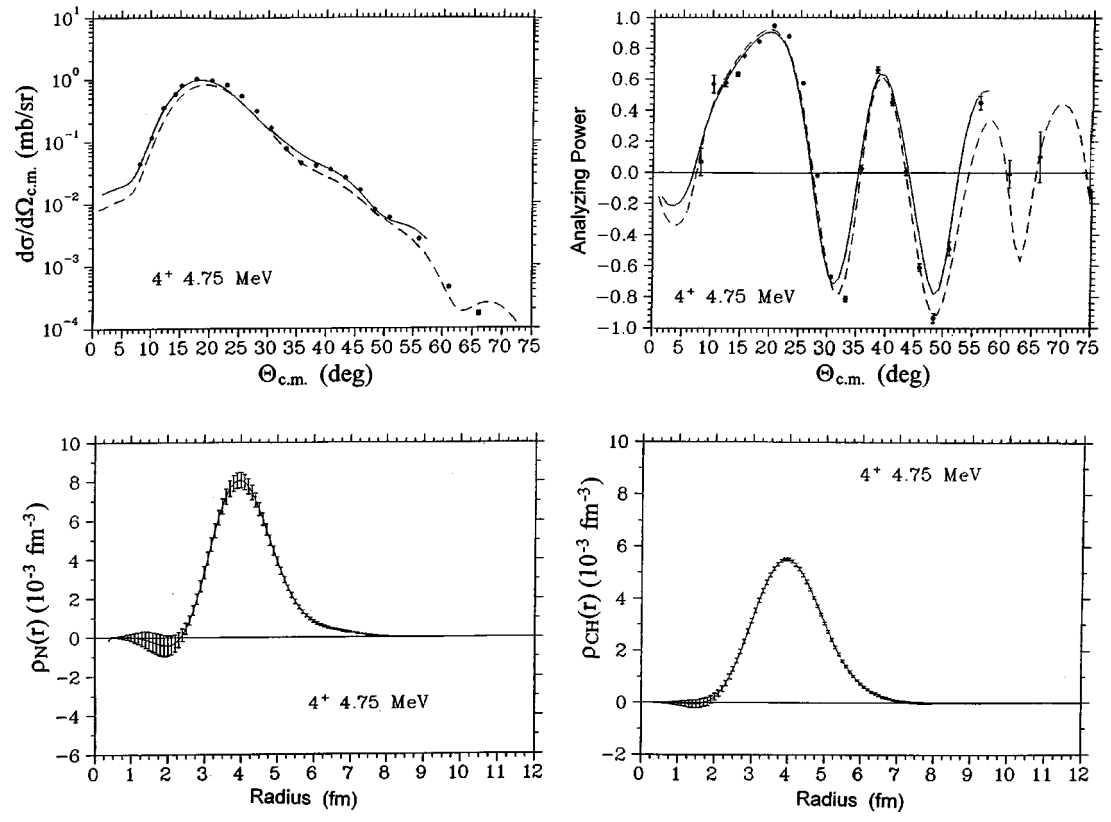

FIG. 11. Cross section and analyzing power data for the 4^+ state at 4.75 MeV, figure description the same as Fig. 2.

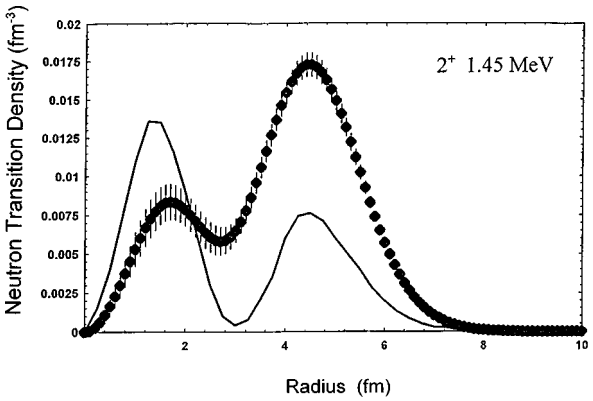

FIG. 12. Neutron transition densities for the 2^+, 1.45 MeV state. The dots with error bars are from the best fit to the present data. The solid line is the result of an energy density calculation from Ref. [29].

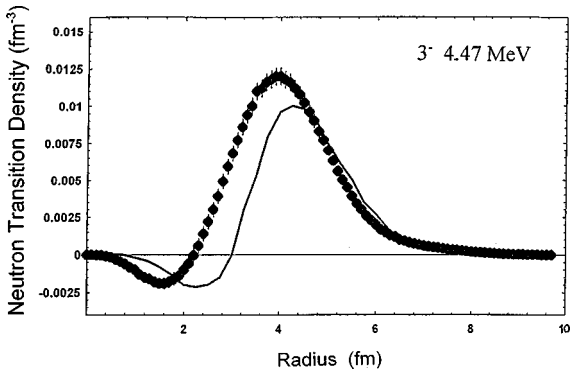

FIG. 13. Neutron transition densities for the 3^-, 4.47 MeV state. The dots with error bars are from the best fit to the present data. The solid line is the result of an energy density calculation from Ref. [29].

nuclear surface. These oscillations are small, but may influence the shape of the neutron transition densities. To minimize this effect, for each transition we examined plots of $\rho_N(r)r^{L+2}$ (which emphasizes the surface) and tried to keep oscillations at large r as small as possible. The code LEA allows for up to 12 expansion coefficients to be varied. However, it was observed that beyond six terms oscillations at large r became large and were deemed unphysical. While six terms is less than that used in previous work, for all the present transitions studied it gave the most stable results. More details on the fitting scheme employed are discussed in Ref. [25].

IV. DATA AND RESULTS

Neutron transition densities have been determined for four 2^+ states (1.45, 2.77, 3.04, and 3.26 MeV), one 3^- state (4.47 MeV), and five 4^+ states (2.46, 3.62, 4.29, 4.40, and 4.75 MeV). The Laguerre-Gaussian expansion coefficients obtained are given in Table I. The uncertainties listed are a combination of three errors, statistical, incompleteness, and normalization. After the first fit, the data were scaled by $+5\%$ and refit, then scaled by -5% and refit in order to estimate the effects of uncertainty in the normalization of the data. The incompleteness error is associated with the truncation of the Laguerre-Gaussian expansion.

Two calculations are presented in the comparisons to the data for each level. Both calculations employ the PH3 empirical effective interaction, along with charge transition densities from inelastic electron scattering. The difference between the two calculations is in the neutron transition densities. The dashed line calculations are where the neutron transition density was obtained by scaling the charge transition density by N/Z. The solid line calculations are when the neutron density was allowed to vary to fit the data. These calculations extend to approximately 57° since this is the range in momentum transfer where the electron scattering data were obtained.

A. 2^+ states

As shown in Fig. 2, the first 2^+ state at 1.45 MeV has a charge transition density that is Gaussian shaped and centered near 4.2 fm, with a small lobe in the interior. This shape is similar to the shape of the transition potential obtained using the collective model. A collective model analysis of this state describes the data quite well [26]. The dashed curve in Fig. 2, which is the result of using a neutron transition density that is scaled by (N/Z) times the charge transition density, describes the overall shape of the cross section data, but smaller in magnitude at the smaller scattering angles. To make up for this cross section deficit, the neutron transition density must be larger than the charge transition density. The best-fit neutron transition density is centered near 4.5 fm, and it exhibits an interior positive lobe centered near 1.7 fm. Figure 2 shows that while the cross section data are described much better by the best-fit neutron transition density calculation (solid curve), the analyzing power data (especially at the larger angles) are best described by the scaled neutron transition density calculation (dashed curve).

Figure 3 presents results for the 2^+, 2.77 MeV state. This state is a good example of the overall improvement of the best-fit neutron transition density calculation over the scaled calculation. The charge transition density has a positive lobe centered near 3.6 fm and a smaller negative lobe centered near 1.5 fm. Also, there is smaller oscillation beyond 5 fm. Therefore, one would expect the cross section data to appear quite different from that of the 1.45-MeV surface-peaked transition, and it is. The fitted neutron transition density is similar in shape to the charge transition density, but larger in magnitude, especially in the oscillation beyond 5 fm.

The 3.04 MeV state shown in Fig. 4 has a charge transition density shape that is between the 1.45 and 2.77 MeV shapes. The largest lobe is positive and centered near 4.1 fm, and there is a negative lobe centered near 1.8 fm. The scaled calculation is similar in shape to the fitted calculation at the smaller scattering angles, as is expected due to the similarity in the surface peaked lobes. The neutron transition density has a larger negative interior lobe than the charge transition density, and this may be reflected in the differences between the two calculations in describing the cross section data.

The data and calculation for the 3.26 MeV state are presented in Fig. 5. The charge transition density is a positive Gaussian centered near 4 fm; this is the only structure. The fitted neutron transition density mainly consists of a positive lobe centered near 3.5 fm; there is also a smaller negative lobe centered near 1.3 fm.

In all four cases the fitted calculation best describes the cross section data, particularly the 2.77 MeV state. The fitted calculation also best describes the analyzing power out to about 35°; beyond that, the scaled calculation does a better job in describing the data.

B. 3^- state

Figure 6 presents results for the only 3^- state analyzed, and it is located at 4.47 MeV. The charge transition density shape consists only of a positive lobe near 4.2 MeV. The fitted neutron transition density mainly consists of a positive lobe centered near 4.0 fm with a smaller negative lobe centered near 1.6 fm. Again, the cross section data are best described by the fitted calculation. At the smaller angles the analyzing power is described equally well by both calculations; however, as with the 2^+ states, the larger angle data are best described by the scaled calculation.

C. 4^+ states

Five 4^+ states have been analyzed; these are located at 2.46, 3.62, 4.29, 4.40, and 4.75 MeV. Results for the 2.46 MeV state are presented in Fig. 7. The charge transition density has a positive lobe centered near 4.4 fm with a smaller negative lobe centered near 2.2 fm. The fitted neutron transition density has a positive lobe centered near 4.1 fm with a much smaller negative lobe centered near 2.1 fm. The cross section data are best described by the fitted calculation. The two calculations for the analyzing power are more similar to each other than they were for the 2^+ and 3^- states; both describe the data equally well. The magnitude of the positive lobe for the neutron transition density is about twice as large as the charge transition density. This is reflected in the calculations for the cross section where the scaled calculation is much smaller in magnitude than the data.

Results for the 3.62 MeV state are presented in Fig. 8. The positive surface-peaked lobe for the charge transition density is centered near 4.1 fm with a smaller negative lobe centered near 1.8 fm. The fitted neutron transition density has a large positive lobe located near 4 fm, and incorporating the error band in the interior, this is the only structure. Unlike the other states previously mentioned, the cross section data at the smaller angles are best described by the scaled calculation, while the analyzing power data are slightly better described by the fitted calculation.

Figure 9 presents the results for the 4.29 MeV state whose charge transition density is similar to the 2.46 MeV state, with a positive surface lobe centered near 4.25 fm with a negative interior lobe located near 2.1 fm. The charge transition density also exhibits a small oscillation beyond 7 fm, which may influence the neutron transition density. The fitted neutron transition density is a single positive lobe centered near 4.1 fm. Both the cross section and the analyzing power data are best reproduced by the fitted calculation.

The 4.40 MeV state results are presented in Fig. 10. The charge transition density surface peaked lobe is centered near 4.1 fm, with the much smaller interior lobe being negative and centered near 2.0 fm. The neutron transition density has a positive surface peaked lobe centered near 3.8 fm with a negative interior lobe centered near 1.8 fm and about a factor of 4 larger than the interior lobe of the charge transition density. Again, the smaller angle cross section data are better described by the fitted calculation, while the larger angle analyzing power data are best described by the scaled calculation.

The final 4^+ state analyzed is presented in Fig. 11. The charge transition density consists of a single surface-peaked lobe centered near 4.0 fm. The fitted neutron transition density is also a single surface-peaked lobe centered near 4.0 fm with a tail extending to larger radii. Again, the cross section data are best described by the fitted calculation, while the analyzing power data are described equally well by both calculations.

D. Multipole matrix elements

The multipole matrix elements are defined as

$$M_{n,p} = \int \rho_{\mathrm{tr}}^{n,p}(r) r^{L+2} dr, \tag{2}$$

with $\rho_{\mathrm{tr}}^{n,p}(r)$ being the neutron or proton transition density and L is the angular momentum transfer and can be used to give an indication of the isospin character of the state. An isoscalar transition has $M_n/M_p = N/Z$: deviation from this value can then be used to characterize a state as being either ''protonlike'' ($M_n/M_p < N/Z$) or ''neutronlike'' ($M_n/M_p > N/Z$). In our analysis the proton transition density is obtained from electron scattering, while the neutron transition density is obtained from a best fit to the inelastic proton scattering data determined in the present work. Table II presents our results for the multipole matrix elements along with the results of collective model analyses from Refs. [18] and [27]. The last column presents results based on an analysis of pion inelastic scattering [28].

Our values of M_n/M_p for the lowest 2^+, 1.45 MeV; 3^-, 4.47 MeV; and 4^+, 2.46 MeV states are larger than those obtained using the collective model. The scaled neutron transition density calculations when compared to the cross section data for these three states are all smaller in magnitude than the data at the first maximum. Therefore, one would expect M_n/M_p to be larger than the isoscalar M_n/M_p value of $N/Z = 1.07$. The pion scattering results (which include only the 2^+, 1.45 MeV and 3^-, 4.47 MeV states) are much closer to our results for proton scattering. In the remaining states (where comparisons can be made), the values of M_n/M_p are in fair agreement (though larger), and the scaled calculations are near the best-fit calculations at the first maximum in the cross section. An earlier microscopic analysis [24] of the 2^+ states at 1.45, 3.04, and 3.26 MeV and 4^+ states at 2.46, 3.63, and 4.75 MeV obtained reduced transition probabilities B (EL) for these states that agree with inelastic electron scattering results [16]. However, in order to match the cross section data [24], the calculations, which assumed $\rho_n(r) = N/Z\rho_p(r)$, had to be scaled by 1.4 for the 2^+, 1.45 MeV state, 1.25 for the 4^+, 2.46 MeV state, and 1.34 for the 4^+, 4.75 MeV state. It is unclear at this time why for some states the scaled cross section calculations are much smaller than the data. It may be that these states are much more neutronlike and are not well represented by the isoscalar assumption implicit in the N/Z scaling procedure.

E. Comparison with calculations based on the energy density method

Lombard and Mas have applied the energy density method in calculating excitation energies, proton and neutron transition probabilities and radial shapes for proton and neutron transition densities for the lowest lying 2^+ and 3^- states for nuclei with N or $Z=20$, 28, 50, 82, and 126 [29]. They use transition densities rather than wave functions to describe the excitation and constrain them to satisfy a sum rule, along with fixing the energies of the isoscalar quadrupole and octupole resonances.

Figures 12 and 13 present our best-fit neutron transition densities with those calculated by Lombard and Mas. For the 2^+, 1.45 MeV state, the calculated shape is similar to the fitted neutron transition density and even obtains a large positive interior lobe. The calculation for the 3^-, 4.47 MeV state is similar in shape to the fitted neutron transition density, but is smaller in magnitude, and the interior lobe peaks at a larger radius.

V. SUMMARY AND CONCLUSIONS

Data have been obtained for 200 MeV polarized proton scattering from ^{58}Ni covering a large range in both excitation energy and scattering angles. Using the code LEA along with an empirical effective interaction and charge transition densities obtained from electron scattering, neutron transition densities have been obtained for four 2^+, one 3^-, and five 4^+ low lying states. Two types of calculations have been performed to compare to the cross section and analyzing power data. One is where the neutron transition densities are scaled by N/Z to that of the charge transition densities, and the other is where the neutron transition density is allowed to vary to fit to the data. In all cases except for one state, the fitted calculations best describe the cross section data and the smaller angle analyzing power data. The scaled calculation generally describes best the large angle analyzing power data. The peak of the neutron transition density in all cases except one occurs at the same or smaller radii in comparison to the charge transition density.

Multipole matrix elements have been obtained and their ratios compared to collective model and pion scattering analyses. In general, our ratios of M_n/M_p are larger than the collective model analysis. The pion results are larger than the collective model results.

The lowest lying 2^+ and 3^- neutron transition density shapes were compared to those calculated by using the energy density method. These calculations qualitatively describe the shapes and size of the extracted neutron transition densities. It would be interesting to have other model calculations of the neutron transition densities to compare to the present results.

ACKNOWLEDGMENTS

The authors would like to thank Prof. James Kelly and Dr. Alan Feldman for assistance in setting up LEA to perform searches on neutron transition densities. This work was supported in part by the National Science Foundation and the Research Corporation.

[1] J. Heisenberg, Adv. Nucl. Phys. **12**, 61 (1981).
[2] J. J. Kelly, W. Bertozzi, T. N. Buti, J. M. Finn, F. W. Hersman, C. Hyde-Wright, M. V. Hynes, M. A. Kovash, B. Murdock, B. E. Norum, B. Pugh, F. N. Rad, A. D. Bacher, G. T. Emery, C. C. Foster, W. P. Jones, D. W. Miller, B. L. Berman, W. G. Love, J. A. Carr, and F. Petrovich, Phys. Rev. C **39**, 1222 (1989).
[3] James J. Kelly, Phys. Rev. C **39**, 2120 (1989).
[4] J. J. Kelly, J. M. Finn, W. Bertozzi, T. Buti, F. W. Hersman, C. Hyde-Wright, M. V. Hynes, M. A. Kovash, B. Murdock, P. Ulmer, A. D. Bacher, G. T. Emery, C. C. Foster, W. P. Jones, D. W. Miller, and B. L. Berman, Phys. Rev. C **41**, 2504 (1990).
[5] J. J. Kelly, A. E. Feldman, B. S. Flanders, H. Seifert, D. Lopiano, B. Aas, A. Azizi, G. Igo, G. Weston, C. Whitten, A. Wong, M. V. Hynes, J. McCelland, W. Bertozzi, J. M. Finn, C. E. Hyde-Wright, R. W. Lourie, P. E. Ulmer, B. Norum, and B. L. Berman, Phys. Rev. C **43**, 1272 (1991).
[6] B. S. Flanders, J. J. Kelly, H. Seifert, D. Lopiano, B. Aas, A. Azizi, G. Igo, G. Weston, C. Whitten, A. Wong, M. V. Hynes, J. McClelland, W. Bertozzi, J. M. Finn, C. E. Hyde-Wright, R. W. Lourie, B. E. Norum, P. Ulmer, and B. L. Berman, Phys. Rev. C **43**, 2103 (1991).
[7] J. J. Kelly, P. Boberg, A. E. Feldman, B. S. Flanders, M. A. Khandaker, S. D. Hyman, H. Seifert, P. Karen, B. E. Norum, P. Welch, S. Nanda, and A. Saha, Phys. Rev. C **44**, 2602 (1991).
[8] H. Seifert, J. J. Kelly, A. E. Feldman, B. S. Flanders, M. A. Khandaker, Q. Chen, A. D. Bacher, G. P. A. Berg, E. J. Stephenson, P. Karen, B. E. Norum, P. Welch, and A. Scott, Phys. Rev. C **47**, 1615 (1993).
[9] J. Kelly, W. Bertozzi, T. N. Buti, J. M. Finn, F. W. Hersman, M. V. Hynes, C. Hyde-Wright, B. E. Norum, A. D. Bacher, G. T. Emery, C. C. Foster, W. P. Jones, D. W. Miller, B. L. Berman, J. A. Carr, and F. Petrovich, Phys. Lett. **169B**, 157 (1986).
[10] J. J. Kelly, Q. Chen, P. P. Singh, M. C. Radhakrishna, W. P. Jones, and H. Nann, Phys. Rev. C **41**, 2525 (1990).
[11] M. A. Khandaker, J. J. Kelly, P. Boberg, A. E. Feldman, B. S. Flanders, S. Hyman, H. Seifert, P. Karen, B. E. Norum, P. Welsh, S. Nanda, and A. Saha, Phys. Rev. C **44**, 1978 (1991).
[12] A. E. Feldman, J. J. Kelly, B. S. Flanders, M. A. Khandaker, H. Seifert, P. Boberg, S. D. Hyman, P. H. Karen, B. E. P. Welsh, Q. Chen, A. D. Bacher, G. P. A. Berg, E. J. Stephenson, S. Nanda, A. Saha, and A. Scott, Phys. Rev. C **49**, 2068 (1994).
[13] J. J. Kelly, B. S. Flanders, F. W. Hersman, J. H. Heisenberg, J. Calarco, J. P. Connelly, T. E. Milliman, A. Scott, F. T. Baker, V. Penumetcha, W. P. Jones, G. T. Emery, A. D. Bacher, C. Olmer, M. A. Grimm, and M. L. Whiten, Phys. Rev. C **47**, 2146 (1993).
[14] E. J. Stephenson, A. D. Bacher, G. P. A. Berg, V. R. Cupps, C. C. Foster, N. Hodiwalla, P. Li, J. Lisantti, D. A. Low, D. W.

Miller, C. Olmer, A. K. Opper, B. K. Park, R. Sawafta, and S. W. Wissink, Phys. Rev. C **42**, 2562 (1990).
[15] Jian Liu, E. J. Stephenson, A. D. Bacher, S. M. Bowyer, S. Chang, C. Olmer, S. P. Wells, S. W. Wissink, and J. Lisantti, Phys. Rev. C **53**, 1711 (1996).
[16] H. P. Blok, Ph.D. thesis Vrije Universiteit te Amsterdam, 1986; (private communication).
[17] S. P. Wells, S. W. Wissink, A. D. Bacher, S. M. Bowyer, S. Chang, J. Lisantti, J. Liu, C. Olmer, A. K. Opper, T. Rinckel, and E. J. Stephenson, Nucl. Instrum. Methods Phys. Res. A **325**, 205 (1993).
[18] J. Lisantti, D. K. McDaniels, Z. Tang, Z. Xu, D. M. Drake, K. H. Hicks, M. C Vetterli, L. W. Swenson, X. Y. Chen, and F. Farzanpay, Nucl. Phys. **A511**, 643 (1990).
[19] J. J. Kelly, computer code LEA, 1990.
[20] H. De Vries, C. W. De Jager, and C. De Vries, At. Data Nucl. Data Tables **36**, 495 (1987).
[21] G. Beuscher, Ph.D. thesis, University of Mainz, 1983.
[22] H. Blok (private communication).
[23] T. Cheon, K. Takayanagi, and K. Yazaki, Nucl. Phys. **A437**, 301 (1985).
[24] Jerry E. Lisantti, Nucl. Phys. **A529**, 682 (1991).
[25] Alan E. Feldman, Ph.D. thesis, University of Maryland, 1991.
[26] J. Lisantti (unpublished).
[27] M. M. Gazzaly, N. M. Hintz, G. S. Kyle, R. K. Owen, G. W. Hoffmann, M. Barlett, and G. Blanpied, Phys. Rev. C **25**, 408 (1982).
[28] R. J. Peterson, Phys. Rev. C **48**, 1128 (1993).
[29] R. J. Lombard and D. Mas, Ann. Phys. (N.Y.) **167**, 2 (1986).